Supplementary Information (SI) for Chemical Science.
This journal is © The Royal Society of Chemistry 2026

Supporting Information

For

NH_4^+-mediated interfacial chemistry for collaborative dual-pathway high-mass-loading energy storage

Jinxin Wang‡, Wei Guo‡*, Mingming Sun, Geng Zhang, Mengting Cheng, Wenbin Xie, Na Hu, Yuehan Yang, and Qiuyu Zhang*

Key Laboratory of Special Functional and Smart Polymer Materials of Ministry of Industry and Information Technology

School of Chemistry and Chemical Engineering

Northwestern Polytechnical University

Xi'an 710129, P. R. China

E-mail: weiguo-nwpu@nwpu.edu.cn (W. Guo); qyzhang@nwpu.edu.cn (Q. Zhang)

‡ These authors contributed equally to this work.

Table of Contents

Experimental Section

Fabrication of Rec-NM-MnO_2 electrode

The P-Mn_3O_4@C electrode was firstly prepared by following our previous work.[1] Then it was electrochemically activated into MnO_2 through 30 CV cycles in 1 M $NaNO_3$ aqueous electrolyte with the P-Mn_3O_4@C, an Ag/AgCl electrode and a Pt sheet electrode (20 × 20 × 0.1 mm^3) as the working, reference and counter electrode, respectively.

Next, the CV-based activation was carried out by using the prepared MnO_2 electrode, an Ag/AgCl electrode and a Pt sheet electrode (20 × 20 × 0.1 mm^3) as the working, reference and counter electrode, respectively. This activation process was performed by 60 CV cycles at 10 mV s^{-1} in the voltage of 0-1.2 V (vs. Ag/AgCl) in the 0.5 M $(NH_4)_2SO_4$/0.5 M $Mn(NO_3)_2$ electrolyte. The activation of control groups was in the similar way, except for the substrates or electrolytes adjusted as needed.

Materials characterization

The as-made materials were characterized by field emission SEM (FEI Verios G4), TEM and HR-TEM (FEI Talos F200X), XRD (Bruker, D8 Advance, Cu-Kα, λ=0.15406 nm), Raman spectroscopy (HORIBA LabRAM HR Evolution), XPS (Kratos AXIS Ultra DLD), FTIR (Bruker Tensor27). X-ray absorption fine structure (XAFS) spectroscopy data was collected in transmission (or fluorescence) mode at 10 kV and 20 mA by the *RapidXAFS* 2M (produced by Anhui Absorption Spectroscopy Analysis Instrument Co., Ltd.). Among them, the analysis of Mn element was carried out using a Si (440) spherical bent crystal analyzer, which has a radius of curvature of 500 mm.

Electrochemical characterization

The electrochemical performances of as-made electrodes were examined with a Corrtest electrochemical workstation (CS310) in a three-electrode cell in 0.5 M $(NH_4)_2SO_4$ and 0.5 M $Mn(NO_3)_2$ mixed electrolyte (when other electrolytes are used, relevant annotations will be given in the text), with an Ag/AgCl electrode and a Pt sheet

electrode ($20 \times 20 \times 0.1$ mm^3) as the reference and counter electrode, respectively. The areal capacitance (C_s, F cm^{-2}) was obtained based by the following equation:

$$C_s=(I\Delta t)/(S\Delta V) \quad (1)$$

Here, I, Δt, ΔV, S represent the discharge current (A), the discharge time (s), the voltage range after an ohmic drop (V), and the effective area of electrodes (cm^2), respectively.

Computation methods

The Vienna Ab Initio Package (VASP) was employed to perform all the density functional theory (DFT) calculations within the generalized gradient approximation (GGA) using the Perdew, Burke, and Enzerhof (PBE) formulation.[2-4] The projected augmented wave (PAW) potentials were applied to describe the ionic cores and take valence electrons into account using a plane wave basis set with a kinetic energy cutoff of 450 eV.[5, 6] Partial occupancies of the Kohn-Sham orbitals were allowed using the Gaussian smearing method and a width of 0.05 eV. The electronic energy was considered self-consistent when the energy change was smaller than 10^{-5} eV. A geometry optimization was considered convergent when the force change was smaller than 0.05 eV/Å. In our structure, the U correction is used for Mn (4.8 eV). Grimme's DFT-D3 methodology was used to describe the dispersion interactions.[7] The vacuum spacing perpendicular to the plane of the structure is 20 Å. The Brillouin zone integral utilized the surfaces structures of 2×2×1 Monkhorst-Pack K-point sampling. Finally, the adsorption energies (E_{ads}) were calculated as $E_{ads} = E_{ad/sub} - E_{ad} - E_{sub}$, where $E_{ad/sub}$, E_{ad}, and E_{sub} are the total energies of the optimized adsorbate/substrate system, the adsorbate in the structure, and the clean substrate, respectively. The free energy was calculated using the equation: $G = E_{ads} + ZPE - TS$, where G, E_{ads}, ZPE and TS are the free energy, total energy from DFT calculations, zero point energy and entropic contributions, respectively.

All XPS data were processed using Casa XPS software. Taking O 1s as an example, the fitting was carried out as follows: 1) A Shirley-type background was subtracted to eliminate the influence of inelastic scattering electrons; 2) The O 1s peak was

deconvoluted into three Gaussian-Lorentzian mixed component peaks; 3) The binding energies of the three components were calibrated and fixed at ~530.1 eV (Mn-O-Mn bond), ~531.6 eV (Mn-OH bonds), and ~533.2 eV (adsorbed H-O-H); 4) Peak areas were integrated with the full width at half maximum (FWHM) constrained and then the relative content of oxygen-containing species was calculated.

Supplementary Figures

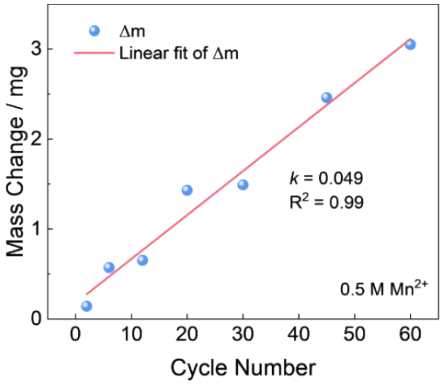

Figure S1. The mass variation of electrodes in different cycles during deposition process in pure 0.5 M $Mn(NO_3)_2$ electrolyte.

Supplementary Note 1

Based on the CV curves in Supplementary Fig. 3c, as the scan rate increased from 5 mV s^{-1} to 30 mV s^{-1}, the calculated capacitive contribution rises from 12% to 36% (Fig. 1f). Besides, the response current density of the main oxidation peak can be fit by the following relationship

$$i=av^b \quad (1)$$

Here, i and v represent the response current and scan rate, respectively. a and b are constants. The b value serves to differentiate between capacitive control (b is close to 1) and diffusion control (b is close to 0.5). For the Rec-NM-MnO_2 electrode, the b value of main oxidation peak is calculated to be 0.52 (Supplementary Fig. 2b). These results suggest a predominantly ion-diffusion-controlled behavior during the charge storage process.

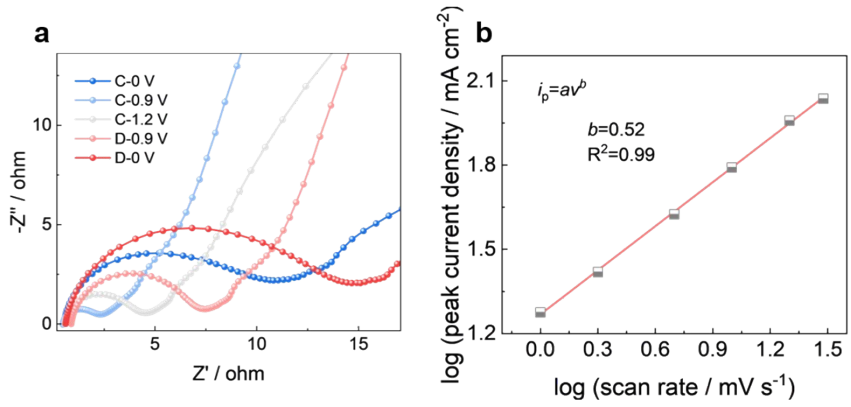

Figure S2. (a) *Operando* EIS spectra of Rec-NM-MnO_2 at different charged and discharged states. (b) Linear relationship between logarithm of the peak current density and logarithm of scan rate for the Rec-NM-MnO_2.

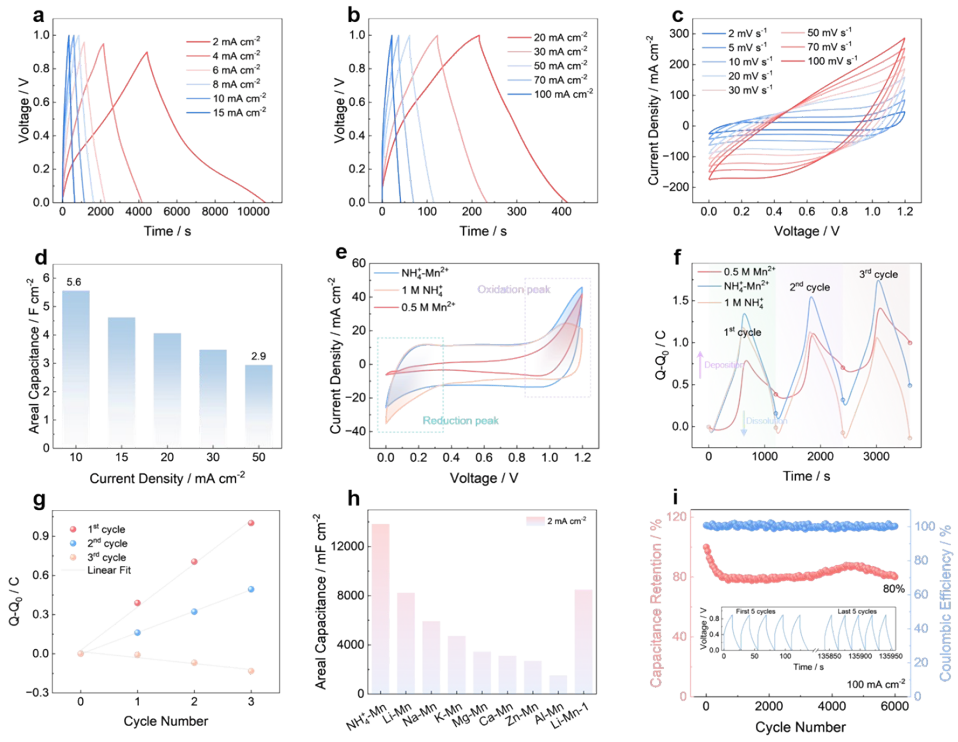

Figure S3. Electrochemical characterization. (a-b) Galvanostatic charge/discharge (GCD) profiles at different current densities, (c) CV curves at different scan rates and (d) areal capacitance at different current densities of Rec-NM-MnO_2 electrode in the NH_4^+-Mn^{2+} mixed electrolyte. (e) CV curves at 2 mV s^{-1} of Rec-NM-MnO_2 electrode in different electrolytes. (f) Charge-time profile and (g) charge variation after different cycles in different electrolyte. (h) Areal capacitance at 2 mA cm^{-2} of the active MnO_2

substrate tested in different mixed electrolytes consisting of 0.5 M $Mn(NO_3)_2$ and other metal salts, e.g., 1 M $(NH_4)_2SO_4$, 2 M $LiNO_3$, 2 M $NaNO_3$, 2 M KNO_3, 1 M $Mg(NO_3)_2$, 1 M $Ca(NO_3)_2$, 1 M $Zn(NO_3)_2$, 0.67 M $Al(NO_3)_3$, and 1 M Li_2SO_4. (i) Cycle performance of Rec-NM-MnO_2 in the NH_4^+-Mn^{2+} mixed electrolyte.

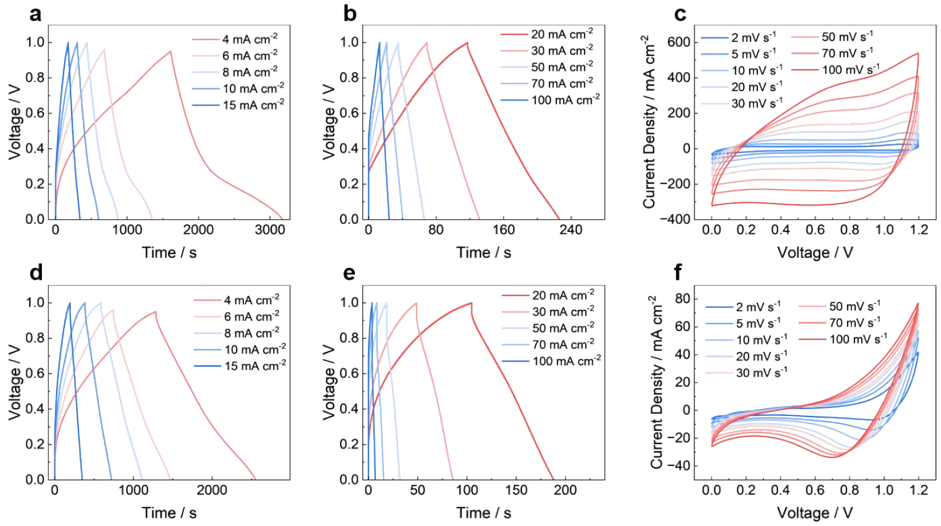

Figure S4. Electrochemical characterization in the different electrolytes. (a-b, d-e) GCD and (c, f) CV curves of the Rec-NM-MnO_2 electrode in (a-c) the 0.5 M $(NH_4)_2SO_4$ electrolyte and (d-f) the 0.5 M $Mn(NO_3)_2$ electrolyte.

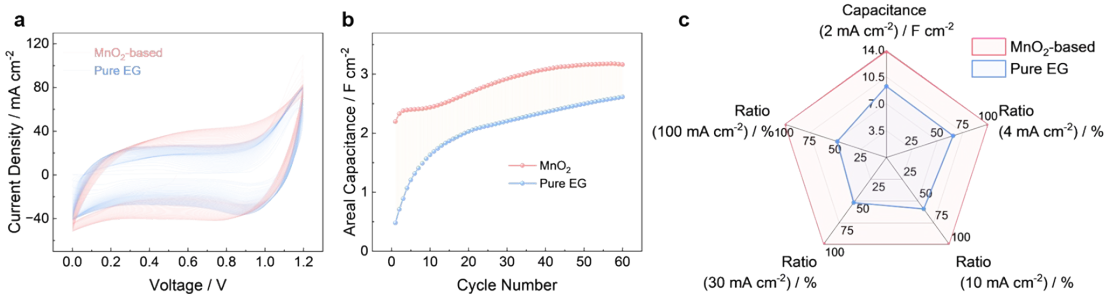

Figure S5. (a) Electrochemical deposition curves and (b) capacitance evolution of different substrates in the NH_4^+-Mn^{2+} mixed electrolyte. (c) Comparison of areal capacitance of different substrates and the capacitance proportion of the pure EG substrate to the active MnO_2-based substrate.

Supplementary Note 2

To evaluate the practical application of the Rec-NM-MnO_2 in NH_4^+-Mn^{2+} mixed electrolyte, an asymmetric supercapacitor was configured in the NH_4^+-Mn^{2+} mixed electrolyte by employing Rec-NM-MnO_2 as the positive electrode (~19 mg cm^{-2}) and the active carbon as the negative electrode (~50 mg cm^{-2}). This asymmetric supercapacitor (ASC) can finely work at a voltage window of 0-1.6 V in the mixed electrolyte at various scan rates of 2-50 mV s^{-1} (Supplementary Fig. 6a). Additionally, this device displays nearly symmetric triangle GCD curves at different current densities of 4-100 mA cm^{-2}, indicating the reversibility during storage energy progress (Supplementary Fig. 6b, c). The device can deliver a high areal capacitance of 3.1 F cm^{-2} at the current density of 4 mA cm^{-2} (Supplementary Fig. 6d). And even the current density increases to 100 mA cm^{-2}, this device can still show a high areal capacitance of 1.5 F cm^{-2} (Supplementary Fig. 6d). It is noteworthy that this device can achieve a maximum energy density of 1070 μWh cm^{-2} at a power density of 3 mW cm^{-2} and a maximum power density of 57 mW cm^{-2} with an energy density of 276 μWh cm^{-2}, which are superior to most previously reported micro supercapacitors (Supplementary Fig. 6e).[8-14] Besides, this device exhibits good cycling stability with a capacity retention of 80% after 500 GCD cycles at a current density of 120 mA cm^{-2} (Supplementary Fig. 6f).

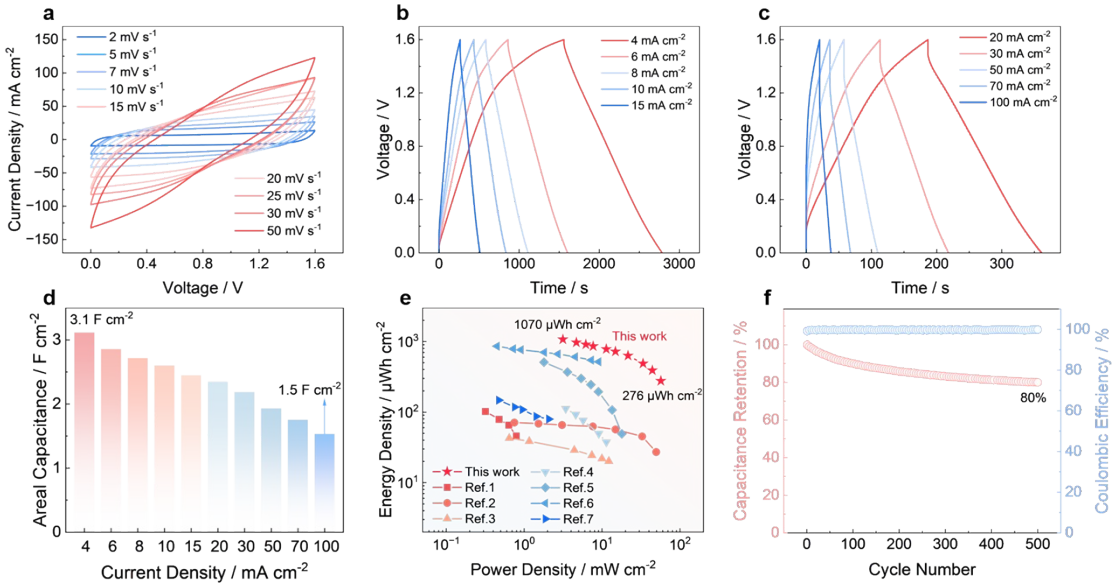

Figure S6. Electrochemical performance of the asymmetric supercapacitor. (a) CV curves at different scan rates. (b-c) Galvanostatic charge/discharge (GCD) profiles at different current densities. (d) Areal capacitance at different current densities. (e) The Ragone plot. (f) Cycle performance.

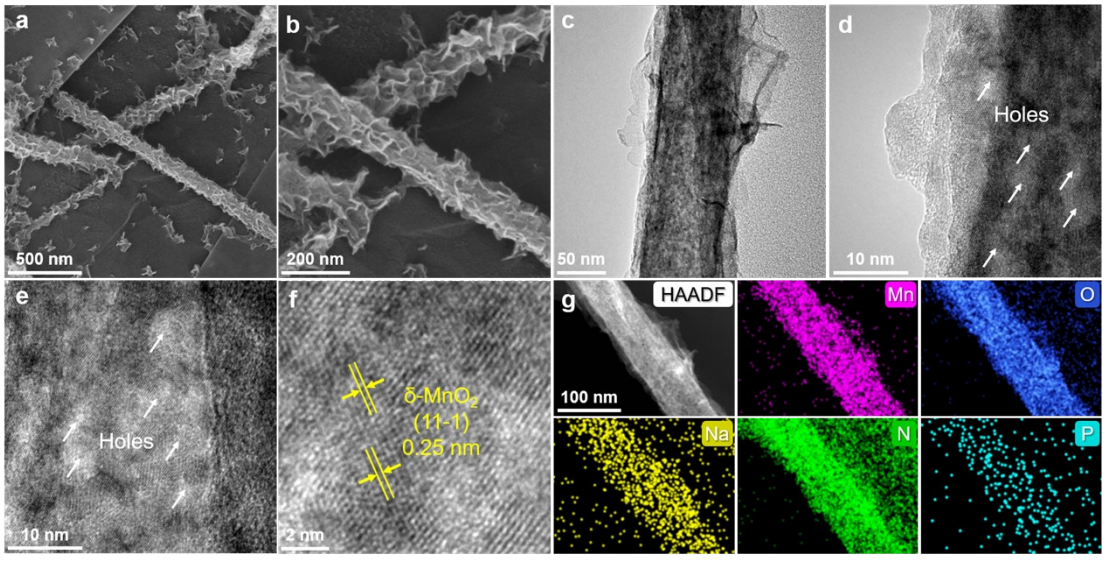

Figure S7. (a-b) SEM, (c-e) TEM, (f) high-resolution TEM, and (g) the corresponding elemental mapping images of the pristine MnO_2 substrate.

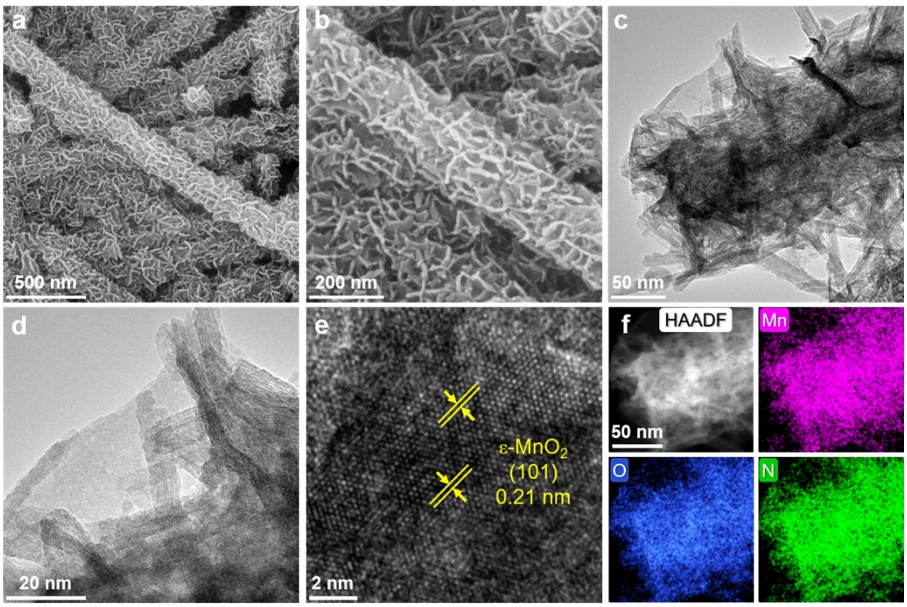

Figure S8. (a-b) SEM, (c-d) TEM, (e) high-resolution TEM, and (f) the corresponding elemental mapping images of Rec-NM-MnO_2.

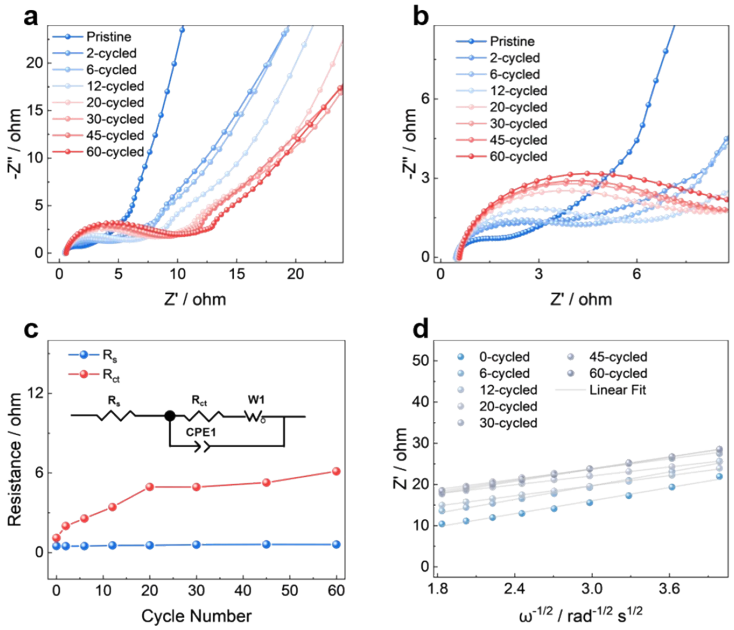

Figure S9. *Operando* EIS characterization of Rec-NM-MnO_2 after different CV cycles. (a-b) Nyquist plots. (c) Variation of R_s and R_{ct}. (d) Linear relationship between the logarithm of peak current density and the logarithm of scan rate.

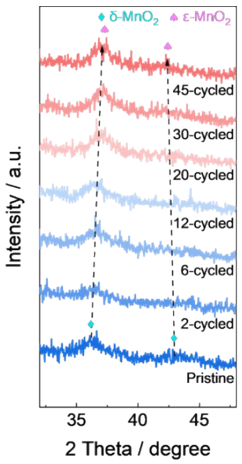

Figure S10. *Ex-situ* XRD patterns of Rec-NM-MnO_2 before and after different CV cycles.

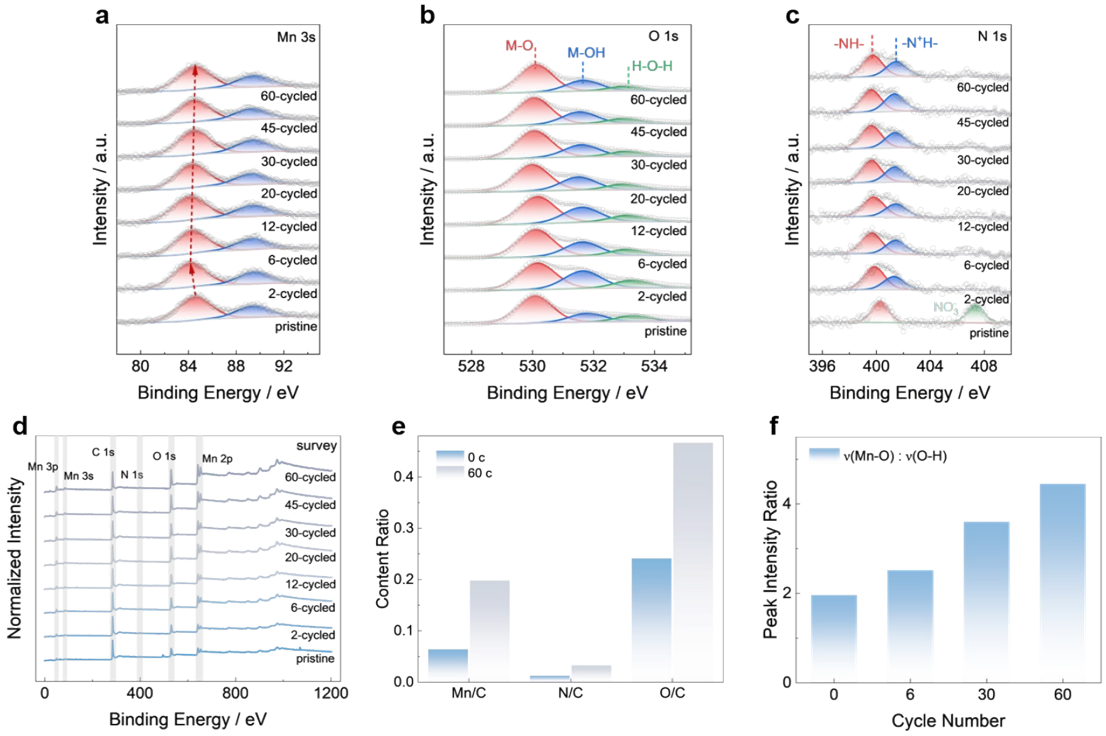

Figure S11. *Ex-situ* XPS spectra of (a) Mn 3s, (b) O 1s, (c) N 1s and (d) full-spectra for Rec-NM-MnO_2 after different CV cycles. (e) The elemental content analysis of Rec-NM-MnO_2 before and after reconstruction. (f) The peak intensity ratio of ν(Mn-O) to ν(O-H) in FTIR spectra of the active MnO_2 substrate during cycling.

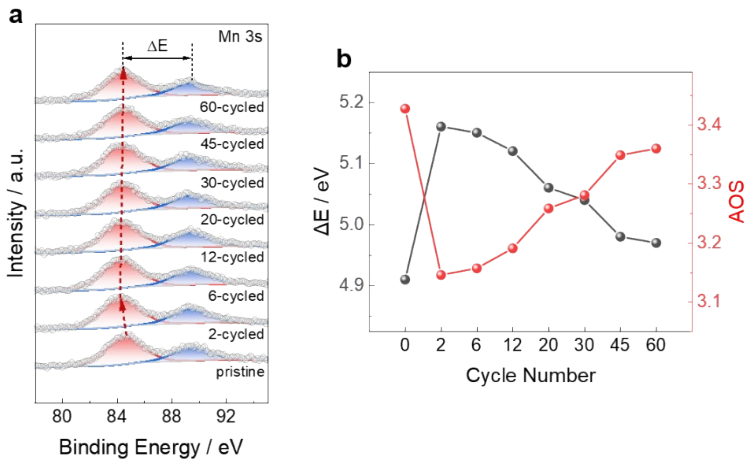

Figure S12. (a) *Ex-situ* XPS spectra of Mn 3s, and (b) the corresponding ΔE value of Mn 3s peaks and AOS of Mn for MnO_2 substrate after different CV cycles in the pure 0.5 M Mn^{2+} electrolyte.

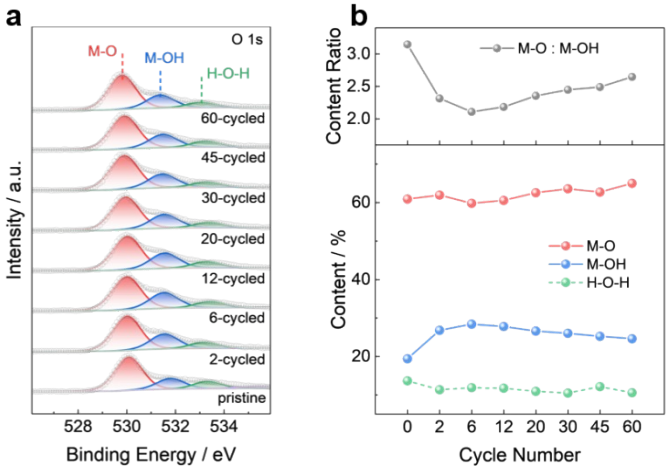

Figure S13. (a) *Ex-situ* XPS spectra of O 1s, and (b) the corresponding content analysis for MnO_2 substrate after different CV cycles in the pure 0.5 M Mn^{2+} electrolyte.

Supplementary Note 3

It is noticed that the diffraction peaks located at 36.2 and 43.0° shifted to higher degrees under a high operation voltage, and then shifted back with the voltage dropping (Supplementary Fig. 14a). This is attributed to the reversible intercalation/deintercalation of cations, e.g., NH_4^+, indicative of reversible carrier storage behavior with the happening of deposition/dissolution process. We also collected the XRD pattern after 60 CV cycles in the pure 0.5 M $Mn(NO_3)_2$ electrolyte, which displays the typical diffraction peaks of ε-MnO_2 (Supplementary Fig. 14c), consistent with that result in the NH_4^+-Mn^{2+} mixed electrolyte. To reduce the interference of the active MnO_2, the *ex-situ* XRD tests were further carried out for the pure EG substrate. Note that the typical diffraction peaks of ε-MnO_2 did not appear until the voltage increases to 1.2 V, indicating that deposition occurred within the voltage of 0.6 to 1.2 V, well consistent with our electrochemical analysis and the literature results (Supplementary Fig. 14b).[15, 16] The similar diffraction peaks reversible shifts during each deposition cycle, further evidencing the happening of the cation storage along with the deposition/dissolution process.

As depicted by the *ex-situ* XPS spectra, the Mn average oxidation state shows a reversible increase/decrease during the first two cycles in the NH_4^+-Mn^{2+} mixed electrolyte (Supplementary Fig. 15). The peak of -N^+H- shows a positive shift of ~0.4 eV to higher energy with charging, and then shift back upon discharging (Supplementary Fig. 16a), implying the reversible deintercalation/intercalation of NH_4^+.[17] Another details is the increase of the content ratio of M-O-M to M-OH bond with charging, and then decreases reversibly with discharging (Supplementary Fig. 16b, c), suggesting the contribution of H^+ as the additional carriers stored, well consistent with the results mentioned before (Fig. 2c and Supplementary Fig. 11b).

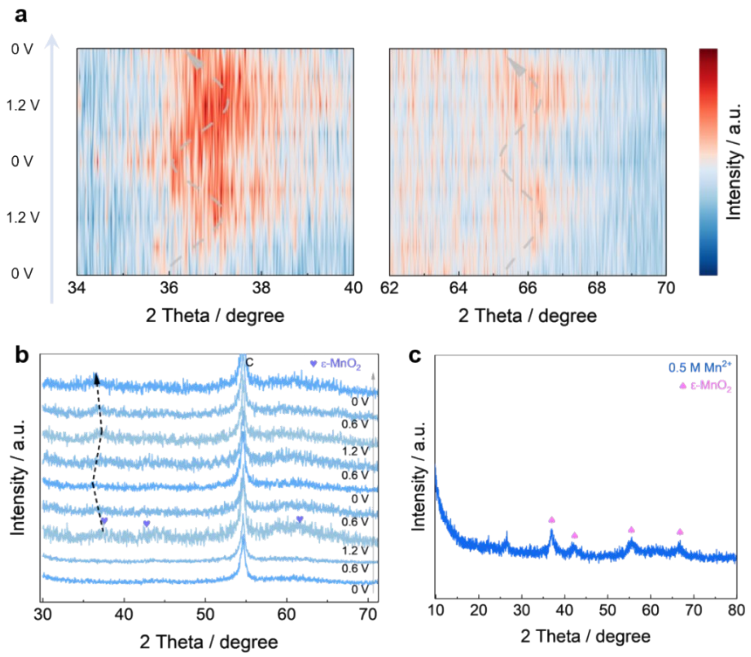

Figure S14. (a) *Ex-situ* XRD patterns of pristine active MnO_2 substrate at different potentials during the first two cycles in the NH_4^+-Mn^{2+} mixed electrolyte. (b) *Ex-situ* XRD patterns of pure EG substrate at different potentials in the first two cycles. (c) XRD pattern of pristine active MnO_2 substrate after 60 CV cycles in the pure 0.5 M $Mn(NO_3)_2$ electrolyte.

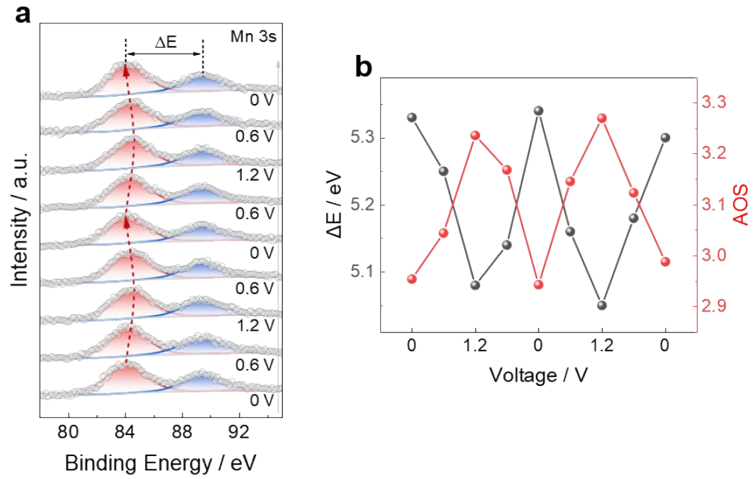

Figure S15. (a) *Ex-situ* XPS spectra of Mn 3s, and (b) the corresponding ΔE value of Mn 3s peaks and AOS of Mn of the active MnO_2 electrode during the first two cycles in the NH_4^+-Mn^{2+} mixed electrolyte.

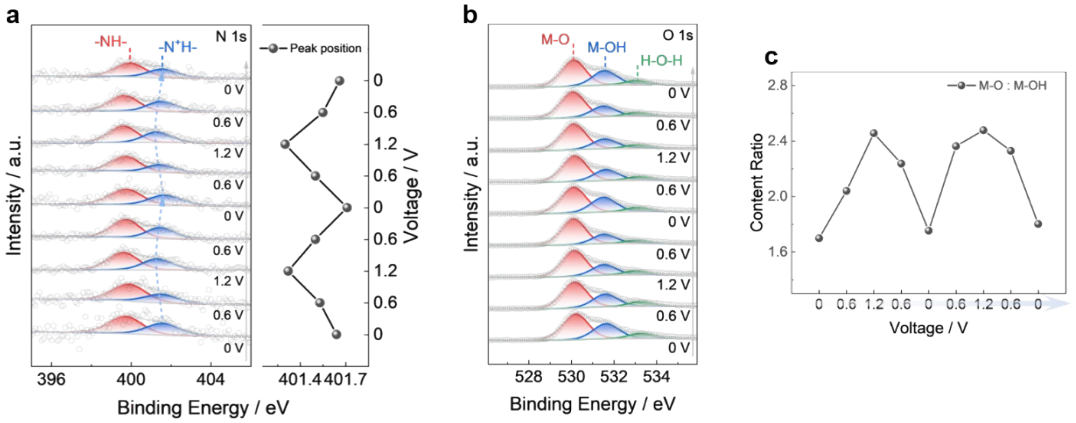

Figure S16. *Ex-situ* XPS spectra of (a) N 1s, and (b) O 1s for the active MnO_2 electrode at different potentials in the first two cycles of deposition process. (c) The corresponding content analysis of the O 1s spectra for Rec-NM-MnO_2.

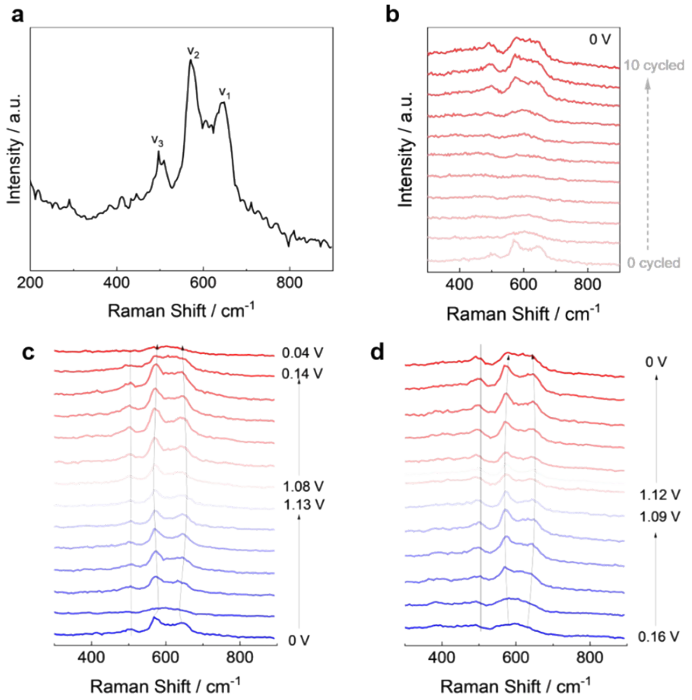

Figure S17. (a) Raman spectra of the pristine MnO_2 substrate. (b) *Operando* Raman spectra of Rec-NM-MnO_2 at 0 V in different CV cycles. (c-d) *Operando* Raman spectra of Rec-NM-MnO_2 at different charged and discharged states in (c) 1st cycle and (d) 10th cycle.

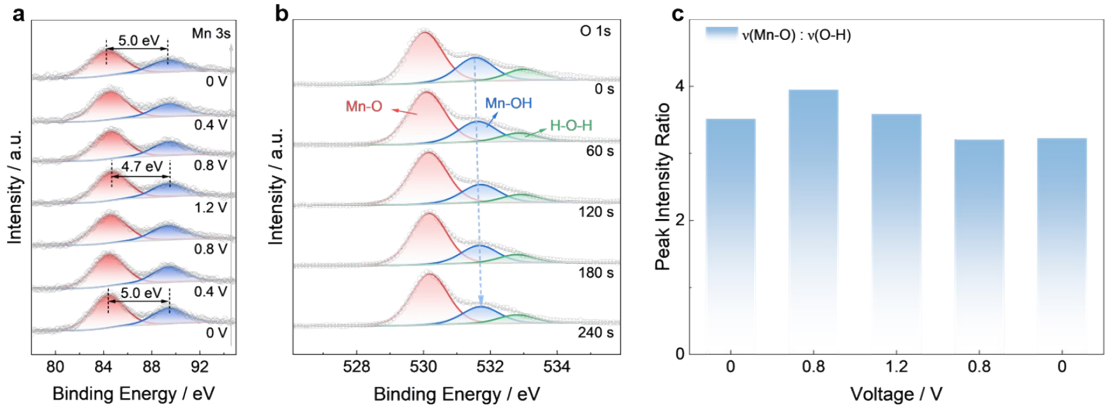

Figure S18. (a) *Ex-situ* XPS spectra of Rec-NM-MnO_2 at different charged/discharged states. (b) O 1s depth profiles of Rec-NM-MnO_2 at the discharged state. The variation range of AOS of Mn (3.30, 3.62) for Rec-NM-MnO_2 is higher than that of the pristine active MnO_2 substrate (2.94, 3.27), originating from the accumulation of ε-MnO_2 with a relatively high valence state upon cycling. (c) The peak intensity ratio of ν(Mn-O) to ν(O-H) in FTIR spectra of the Rec-NM-MnO_2 electrode at different voltages.

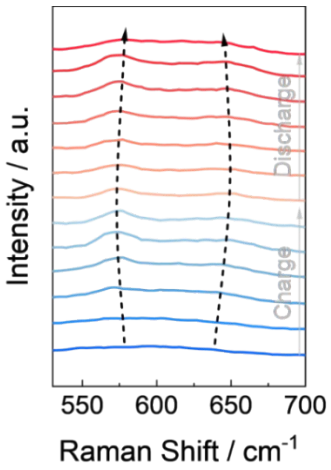

Figure S19. *Operando* Raman spectra in the range of 530 cm^{-1} to 700 cm^{-1} of Rec-NM-MnO_2 at different charged and discharged states.

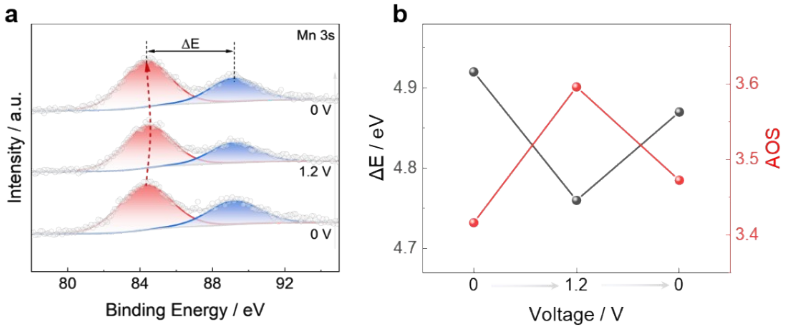

Figure S20. (a) *Ex-situ* XPS spectra of Mn 3s, and (b) the corresponding ΔE value of Mn 3s peaks and AOS of Mn for ε-MnO_2 electrode in the pure 0.5 M Mn^{2+} electrolyte at different charged and discharged states.

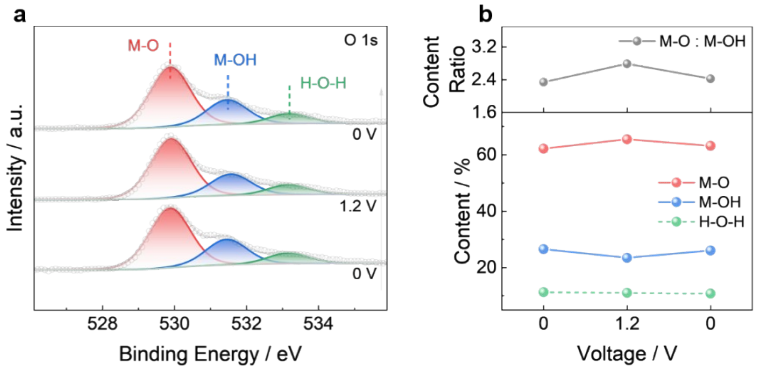

Figure S21. (a) *Ex-situ* XPS spectra of O 1s, and (b) the corresponding content analysis for ε-MnO_2 electrode in the pure 0.5 M Mn^{2+} electrolyte at different charged and discharged states.

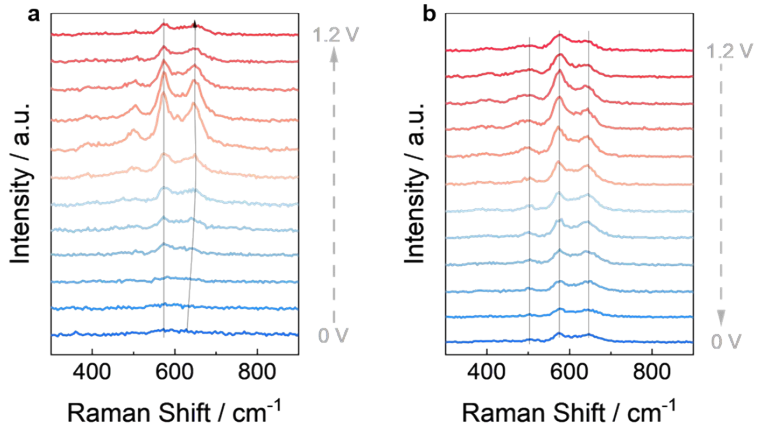

Figure S22. *Operando* Raman spectra of Rec-NM-MnO_2 in the pure 0.5 M $(NH_4)_2SO_4$ electrolyte at different states.

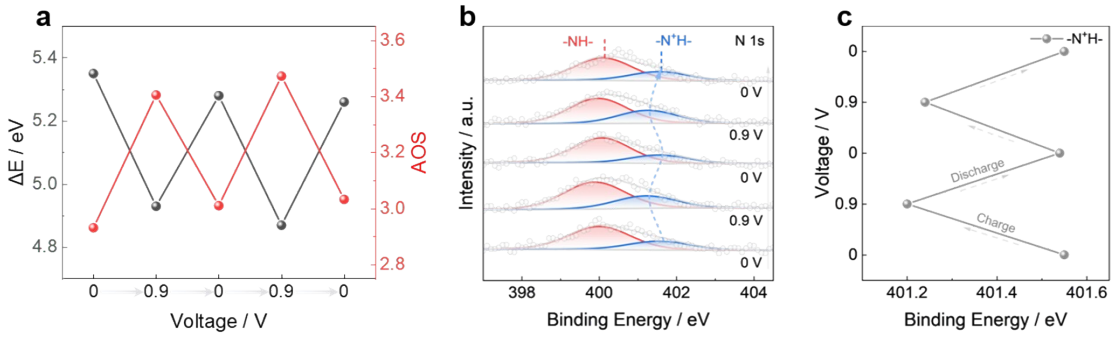

Figure S23. *Ex-situ* XPS characterization of Rec-NM-MnO_2 electrode during the first two GCD cycles in pure 0.5 M $(NH_4)_2SO_4$ electrolyte. (a) Variation of ΔE value of Mn 3s peaks and AOS of Mn. (b) N 1s spectra. (c) Position variation of the peak relative to -N^+H- bond in N 1s spectra.

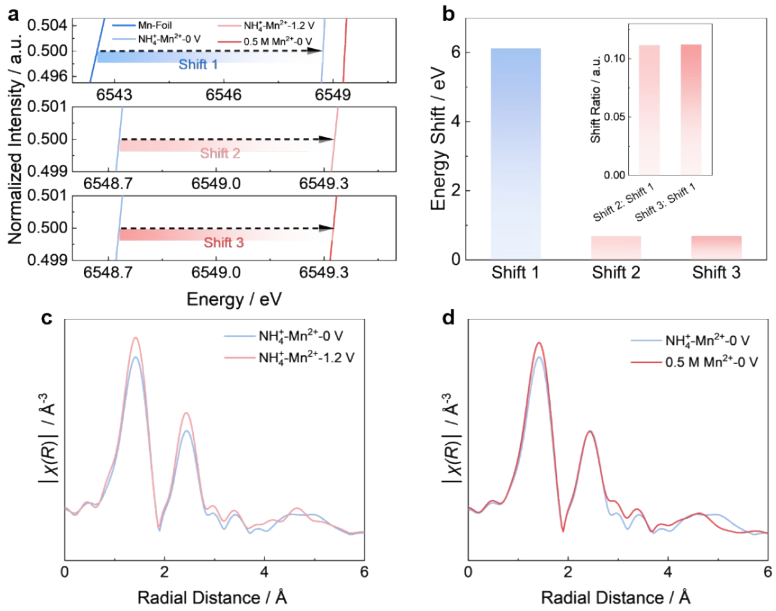

Figure S24. (a-b) Energy shifts in Mn K-edge XANES spectra of Rec-NM-MnO_2 at different charged states in the pure Mn^{2+} and NH_4^+-Mn^{2+} mixed electrolytes. (c-d) Comparison of the k^3-weight Fourier transformation (c) between Rec-NM-MnO_2 at 0 V and Rec-NM-MnO_2 at 1.2 V, as well as (d) between Rec-NM-MnO_2 at 0 V and Mn species fabricated in the pure Mn^{2+} electrolyte at 0 V.

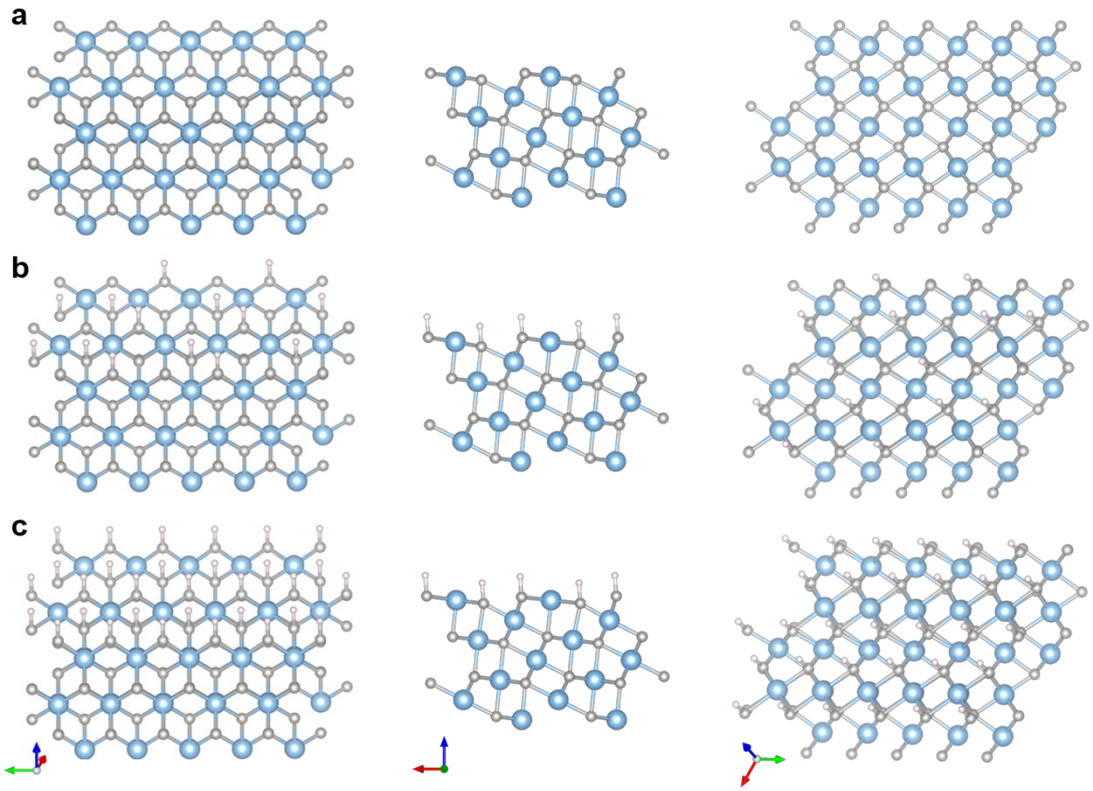

Figure S25. Atomic models of (a) the pure MnO_2, (b) H-MnO_2(p), (c) H-MnO_2(h).

Supporting Table

Table S1. A comparison of capacitance, current density and mass-loading for the Rec-NM-MnO_2 and related results in literature.

Electrode materials	Areal capacitance	Current density	Mass loading	Ref.
Rec-NM-MnO_2	13.8 F cm^{-2}	2 mA cm^{-2}	27.1 mg cm^{-2}	*This work*
Rec-MnO_2 (without NH_4^+)	6.5 F cm^{-2}	2 mA cm^{-2}	24.3 mg cm^{-2}	
O_v–MnO_2	4.8 F cm^{-2}	2 mA cm^{-2}	12 mg cm^{-2}	*Energy Environ. Sci., 2024, 17, 3384-3395*
WC@MnO_2-20	3.6 F cm^{-2}	1 mA cm^{-2}	14.1 mg cm^{-2}	*Small, 2022, 18, 2201307*
δ-MnO_2@CC	5.4 F cm^{-2}	2 mA cm^{-2}	18 mg cm^{-2}	*Adv. Mater., 2022, 34, 2107992*
MnO_2/C	9.4 F cm^{-2}	0.5 mA cm^{-2}	19.7 mg cm^{-2}	*Adv. Funct. Mater., 2021, 31, 2009632*
MnO_2/HGF	7.4 F cm^{-2}	1 mA cm^{-2}	28.2 mg cm^{-2}	*Research, 2020, 2020, 7304767*
NH_4^+-MnO_2@CC	3.8 F cm^{-2}	2 mA cm^{-2}	13 mg cm^{-2}	*J. Energy Storage, 2025, 133, 118001*
Heter-MnO_2-1.38	4.8 F cm^{-2}	1 mA cm^{-2}	30 mg cm^{-2}	*Adv. Energy Mater., 2023, 13, 2300224*
CNF/CNT/MnO_2	3.5 F cm^{-2}	1 mA cm^{-2}	16.8 mg cm^{-2}	*Carbohyd. Polym., 2024, 326, 121661*
InFeMO	1.9 F cm^{-2}	3.2 mA cm^{-2}	10.6 mg cm^{-2}	*J. Mater. Chem. A, 2023, 11, 2133-2144*
MnO_2-60	3 F cm^{-2}	3 mA cm^{-2}	10 mg cm^{-2}	*ACS Nano, 2018, 12, 3557-3567*

Table S2. EIS Fitting results of Rec-NM-MnO_2 electrode after different cycles.

	EIS fitting results						
	R_s / Ω	R_{ct} / Ω	CPE-T	CPE-P	W-R	W-T	W-P
Pristine	0.48983	1.099	2.3961E-4	1.0080	11.71	1.462	0.43480
2-cycled	0.47483	1.996	3.6917E-4	0.96477	14.89	2.843	0.36077

6-cycled	0.48233	2.558	3.4140E-4	0.94868	12.78	3.331	0.35198
12-cycled	0.53433	3.426	2.5393E-4	0.95014	14.01	4.648	0.32748
20-cycled	0.53557	4.947	2.5699E-4	0.92329	15.98	5.862	0.30945
30-cycled	0.59073	4.935	1.8229E-4	0.96071	15.27	4.931	0.28583
45-cycled	0.60612	5.270	1.6953E-4	0.97227	14.53	4.684	0.29419
60-cycled	0.60510	6.121	1.8352E-4	0.96054	16.77	6.495	0.30571

References

1 J. X. Wang, W. Guo, M. M. Sun, G. Zhang, Y. Meng and Q. Y. Zhang, *Energy Environ. Sci.*, 2025, **18**, 960-971.

2 G. Kresse and J. Furthmuller, *Phys. Rev. B*, 1996, **54**, 11169-11186.

3 G. Kresse and D. Joubert, *Phys. Rev. B*, 1999, **59**, 1758-1775.

4 J. P. Perdew, K. Burke and M. Ernzerhof, *Phys. Rev. Lett.*, 1996, **77**, 3865-3868.

5 S. Grimme, J. Antony, S. Ehrlich and H. Krieg, *J. Chem. Phys.*, 2010, **132**, 154104.

6 P. E. Blochl, *Phys. Rev. B*, 1994, **50**, 17953-17979.

7 G. Henkelman, B. P. Uberuaga and H. Jonsson, *J. Chem. Phys.*, 2000, **113**, 9901-9904.

8 F. Y. Xie, Y. Du, M. H. Chu, X. Y. Jia, H. Cao, R. Zhang, H. W. Li and M. Zhang, *Chem. Eng. J.*, 2025, **513**, 162864.

9 Y. J. Lei, W. L. Zhao, Y. P. Zhu, U. Buttner, X. C. Dong and H. N. Alshareef, *ACS Nano*, 2022, **16**, 1974-1985.

10 B. Shi, L. Li, A. B. Chen, T. C. Jen, X. Y. Liu and G. Z. Shen, *Nano-Micro Lett.*, 2022, **14**, 34.

11 L. Naderi and S. Shahrokhian, *Nanoscale*, 2022, **14**, 9150-9168.

12 Z. Y. Han, X. Y. Zhang, G. L. Tang, J. Liang and W. Wu, *J. Energy Storage*, 2024, **91**, 112023.

13 D. D. Ling, D. H. Zhang and Q. F. Wang, *Chem. Eng. J.*, 2025, **520**, 166064.

14 S. J. Xiong, X. X. Li, G. S. Li, Z. L. Wang, Z. J. Wang, M. D. Guo, C. K. Zhang, Y. N. Ma and T. C. Zeng, *Adv. Funct. Mater.*, 2025, **36**, e13738.

15 Y. X. Zhang, A. Y. Hu, D. W. Xia, S. Hwang, S. Sainio, D. Nordlund, F. M. Michel, R. B. Moore, L. X. Li and F. Lin, *Nat. Nanotechnol.*, 2023, **18**, 790-797.

16 X. L. Ye, D. L. Han, G. Y. Jiang, C. J. Cui, Y. Guo, Y. G. Wang, Z. C. Zhang, Z. Weng and Q. H. Yang, *Energy Environ. Sci.*, 2023, **16**, 1016-1023.

17 X. Y. Qi, Y. R. Zhu, Y. T. Xu, W. H. Chen, Z. L. Hu, L. J. Xi, Y. J. Xie, H. S.

Hou, G. Q. Zou and X. B. Ji, *Energy Storage Mater.*, 2025, **75**, 104063.